# Localization of geoid anomalies and the evolution of oceanic lithosphere: A case study from the Mendocino Fracture Zone

C. Cadio[1] and J. Korenaga[1]

[1]   The thermal evolution of oceanic lithosphere is investigated by focusing on geoid offsets occurring across the Mendocino Fracture Zone, where plates with different ages are juxtaposed. Various processing techniques have been devoted to separate the geoid signal of the age contrast from regional and shorter wavelength components unrelated to the thermal structure of lithosphere. Nevertheless, due to processing differences, estimates of geoid offsets vary, and no agreement on the thermal evolution of oceanic lithosphere has been found so far. In this study, we propose to use a continuous wavelet analysis to accurately characterize the components of the geoid at different spatial scales and to estimate a new geoid slope-age relationship from localized signals. We also apply the same wavelet transform on a set of synthetic geoid calculated with different assumptions on plate cooling. The comparison of the observed geoid offsets with those predicted from cooling models indicates that our approach can successfully remove unwanted regional contributions and isolate the geoid signature due to lithospheric cooling. Our results suggest that, contrary to previous studies, geoid slopes measured at the Mendocino Fracture Zone are compatible with both the half-space cooling model and the plate model.

## 1.   Introduction

[2]   Density variations associated with the cooling of oceanic lithosphere contribute significantly to the forces driving the plate motion on the Earth's surface [*Hager*, 1978; *Schubert*, 1980]. Understanding the thermal evolution of oceanic lithosphere is thus crucial to better understand plate tectonics, which is the primary manifestation of large-scale mantle convection. Because temperatures at depth are not directly measurable, much effort has been directed toward modeling the average thermal structure of oceanic lithosphere as a function of age.

[3]   Two classes of simple models, based on the variation of seafloor depth and heat flow with age, have been proposed. In one model, the lithosphere behaves as the upper boundary layer of a cooling half-space [*Turcotte and Oxburgh*, 1967]. The thickness of the lithosphere increases with time, and linear relationships are predicted between depth and the square root of age, and between heat flow and the inverse of the square root of age [*Parker and Oldenburg*, 1973; *Davis and Lister*, 1974]. This model is generally referred to as the

half-space model. In the other model, the lithosphere is treated as a cooling plate with an isothermal lower boundary, such that its thickness approaches a constant value for older ages [*Langseth et al.*, 1966; *McKenzie*, 1967]. In this so-called plate model, an additional source of heat should be present in the mantle to balance heat lost at the seafloor and limit the growth of the lithosphere. Radiogenic heat [*Crough*, 1977; *Forsyth*, 1977], shear stress heating [*Schubert et al.*, 1976], small-scale convection [*Richter and Parsons*, 1975; *Parsons and McKenzie*, 1978], and mantle plumes [*Heestand and Crough*, 1981; *Schroeder*, 1984; *Davies*, 1988] are all possibilities. Discriminating between these two models would thus lead to a better understanding of underlying geodynamical processes and mantle convection in general.

[4]   For young lithosphere, these models give similar predictions, whereas for older ages the plate model implies that seafloor depth and heat flow reach certain equilibrium values. Although such observations have been reported in the past [*Sclater and Francheteau*, 1970; *Parsons and Sclater*, 1977], the relation between this apparent "flattening" in the data and the "normal" thermal evolution of oceanic lithosphere remains controversial [e.g., *Korenaga and Korenaga*, 2008]. Indeed, seafloor flattening can be the natural consequence of another physical mechanism besides cooling, such as dynamic support associated with asthenospheric channel flow [*Phipps Morgan and Smith*, 1992], upwelling plumes [*Heestand and Crough*, 1981; *Schroeder*, 1984; *Davies*, 1988; *Smith and Sandwell*, 1997], or large-scale convective processes of deep-seated origin [*Davies and Pribac*, 1993]. Obviously, seafloor topography is

[1]Department of Geology and Geophysics, Yale University, New Haven, Connecticut, USA.

Corresponding author: C. Cadio, Department of Geology and Geophysics, Yale University, 210 Whitney Ave., New Haven, CT 06511, USA. (cecilia.cadio@yale.edu)

affected by the formation of oceanic islands and plateaus, which could mask subsidence due to half-space cooling, and the older seafloor is more likely to have encountered these anomalous events.

[5] As these models differ in bottom boundary conditions, the predicted thermal structures differ most at depth. The geoid depends on the depth-weighted integral of the density anomaly [*Ockendon and Turcotte*, 1977]. It is thus much more sensitive to thermal perturbations in the lower portion of the lithosphere than ocean depth and heat flow, and would be the best-suited observable for discriminating between these models [e.g., *Sandwell and Schubert*, 1982]. The cooling of lithosphere causes the geoid height to decrease with the age of the ocean floor, linearly with the half-space model [*Haxby and Turcotte*, 1978], or exponentially with the plate model [*Parsons and Richter*, 1980; *Sandwell and Schubert*, 1980]. However, these variations are of long wavelength, hence hard to isolate from unrelated, long-wavelength geoid undulations originating in deep mass variations due to mantle convection.

[6] The geoid anomaly associated with lithospheric cooling, however, may be extracted by estimating a geoid offset across a fracture zone (FZ), which juxtaposes lithosphere of two different ages, and thus of two different thermal structures [*Crough*, 1979]. The density contrast at a fracture zone results in a step-like change in geoid height, which increases from the older to the younger side of the fracture zone. Although this change in geoid height is small (a few tens of centimeters to a few meters), it occurs over a relatively short distance across a fracture zone (one or two hundred kilometers). Thus this signature could easily be distinguished from long-wavelength geoid signals unrelated to cooling. Moreover, if the age offset across a fracture zone is known, a geoid height-age relation can be estimated and compared to predictions by the lithospheric cooling models.

[7] In practice, however, the overall amplitude of a geoid step across a fracture zone is difficult to estimate because it is superimposed upon contributions that are unrelated to the thermal structure of lithosphere. Various processing techniques have been used to separate the geoid signal of the age contrast from regional components [*Crough*, 1979] as well as shorter wavelength components associated with lateral heat flow [*Louden and Forsyth*, 1976], flexure [*Sandwell*, 1984], and thermal stresses [*Parmentier and Haxby*, 1986]. Nevertheless, due to processing differences, estimates for a given fracture zone vary, and no consensus on the thermal evolution of oceanic lithosphere has been reached. Although most of previous studies are in accord with the plate model [e.g., *Detrick*, 1981; *Cazenave et al.*, 1982; *Sandwell and Schubert*, 1982; *Richardson et al.*, 1995], others cannot distinguish between the two models [e.g., *Wessel and Haxby*, 1989] or show that observed geoid steps are not compatible with either of the cooling models [e.g., *Cazenave*, 1984; *Driscoll and Parsons*, 1988; *Marty and Cazenave*, 1988].

[8] One common problem with these different studies is that a significant portion of the data, located in the vicinity of a fracture zone, is ignored in order to avoid biasing the estimate of a geoid step by unwanted regional and local contributions. As a result, just a few points are actually used to estimate an overall geoid offset. In order to better estimate a geoid step, therefore, we propose to use the continuous wavelet analysis (CWT) of geoid anomalies. Such analysis

allows us to unfold the components of the geoid at different spatial scales. In this way, the geoid signature associated with the lithospheric thermal structure can be extracted more accurately from other contributions. Moreover, the regional component, which is the largest source of error in the offset determination [*Detrick*, 1981], can be correctly evaluated. This wavelet approach has already been employed successfully in recent years [*Panet et al.*, 2006, 2007; *Cadio et al.*, 2011, 2012].

[9] In this paper, we estimate geoid anomalies associated with the cooling of oceanic lithosphere from the high-quality GRACE gravity data. In the following sections, we first explain the principle of continuous wavelet analysis and how to extract a geoid slope-age relationship from localized signals. We then describe how to calculate geoid anomalies for different cooling models including, for the first time, the effects of lateral density variations. As a case study, we apply this new approach to the Mendocino FZ, which has been of particular interest among geophysicists for many years. Finally, we discuss the comparison between the observed and synthetic geoid slope-age relationships and their implications for the thermal evolution of oceanic lithosphere.

## 2. CWT and Estimating the Geoid Slope-Age Relation

[10] A CWT provides a redundant and finely detailed description of a signal in terms of both space and wavelength. The CWT is constructed from a set of coefficients as defined from the correlation between the signal and a localizing function called wavelet, at a given spatial scale and position. Because scale and position can vary continuously, such an analysis enables us to finely characterize the features of a given signal across a range of scales [*Holschneider*, 1995]. CWTs are particularly helpful in tackling problems involving the detection of a weak, small-scale component masked by stronger, large-scale contributions and thus not easily detectable by simple visual inspection.

[11] A wavelet is a piecewise continuous function with zero mean and finite energy, well localized both in the spatial and spectral domains. For a given wavelet family, each function is described with two parameters: the position parameter, $e$, defines the point around which the wavelet concentrates its energy in the spatial domain (its center), and the scale parameter, $a$, sets its spatial extent. Wavelets can be regarded as local bandpass filters, with the center of the bandwidth defined by the scale parameter. Here we use spherical Poisson multipole wavelets introduced by *Holschneider et al.* [2003]. Figure 1 represents a cross-section of these wavelets at three different scales, all located at $(0°N, 180°E)$. Such wavelets are particularly well suited to analyze potential fields. Just as spherical harmonics, they are generated by the Legendre polynomials, and the use of the same generating functions allows us to easily analyze geoid anomalies derived from a global spherical harmonics model. Moreover, these wavelets may be identified with multipoles of order $m$ (or equivalent sources). The depth of the multipole is directly related to the scale parameter. In addition to the scale and position parameters, a Poisson multipole wavelet is thus defined by a third parameter: its order $m$. The order parameter characterizes the global shape of a wavelet (the number of oscillations). Increasing $m$
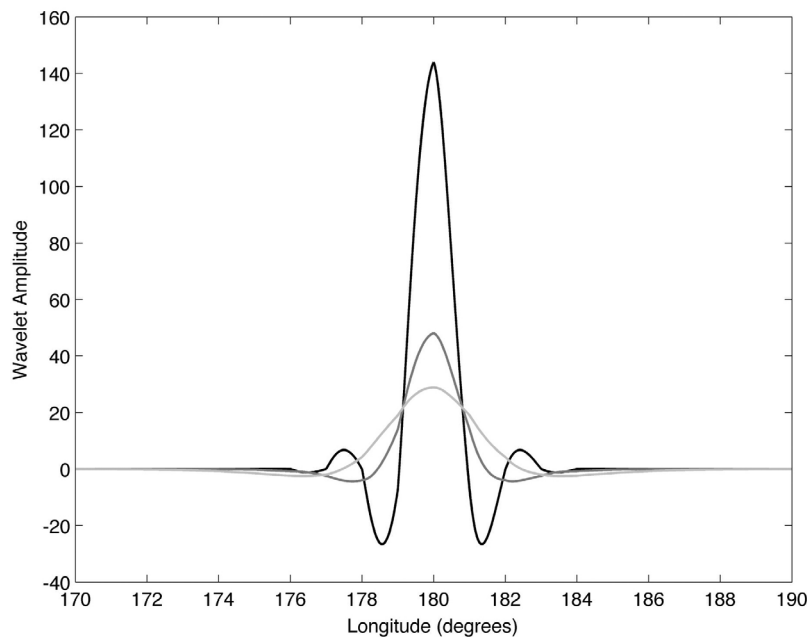
**Figure 1.** Cross section of Poisson multipole wavelets of order 3 and scales 100 km (black line), 300 km (dark-gray line), and 500 km (light-gray line), all centered at (0°N, 180°E).

improves spectral localization but deteriorates spatial localization. A compromise must be found given the spectral properties of a target field. For the gravity field, the order is fixed to 3, allowing satisfactory localization both in space and wavelength [*Chambodut et al.*, 2005]. Different applications of these wavelets are shown in *Panet et al.* [2006, 2007] and *Cadio et al.* [2011, 2012].

[12] In many previous studies, the amplitude of a geoid step is normalized by a corresponding age difference across a fracture zone and plotted as a function of the average age of the two lithospheric segments. This ratio, called the "geoid slope," represents the first-order derivative of the geoid with age. Here the geoid slope is estimated from the ratio of the localized geoid offset to the localized age offset. That is, the geoid slope $\Delta N/\Delta t$ at the scale $a$ and the position $e$ is given by

$$\frac{\Delta N}{\Delta t}(a,e) = \frac{\Delta C_N(a,e)}{\Delta C_t(a,e)}, \qquad (1)$$

where $\Delta C_N$ and $\Delta C_t$ are the difference between maximum and minimum CWT coefficient values across a fracture zone of, respectively, the geoid and the seafloor age. The geoid slope estimated this way can then be compared with predictions from different cooling models, the calculation of which is explained next.

## 3. Models

[13] Assuming an isostatically compensated lithosphere, a theoretical geoid signal has been derived by *Haxby and Turcotte* [1978] for the half-space cooling model, and by *Sandwell and Schubert* [1980] and *Parsons and Richter* [1980] for the plate model. In these analytical solutions,

however, geoid anomalies are related to vertical density distribution only. When comparing observed and theoretical geoid slopes across a fracture zone, such analytical solutions have been directly used in previous studies. That is, a theoretical geoid slope is calculated by analytically differentiating a theoretical geoid with age and compared with an observed geoid slope across a fracture zone. The effect of lateral density variations caused by an age offset at a fracture zone is therefore entirely ignored when calculating a theoretical geoid slope. In order to take into account such effect, we calculate geoid anomalies in the spatial domain considering both lateral and vertical density variations. A model lithosphere is composed of an array of columns, each of which is formed by a vertical stack of constant density prisms (Figure 2). A geoid signal in every surface point of the model space is calculated by adding contributions from all individual prisms.

[14] Each column has a horizontal cross-section of 25 × 25 km, and a depth to each column top is adjusted to maintain an isostatic balance. Within each column, prisms have variable thicknesses, with the maximum of 6 km, and each column continues to the base of the lithosphere, which varies as a function of seafloor age as described later. The $i$-th prism is defined by the Cartesian coordinates $X_1^i$, $X_2^i$, $Y_1^i$, $Y_2^i$, $Z_1^i$, and $Z_2^i$, whereas the computation point $P$ is located at $X_P$, $Y_P$, and $Z_P$ (Figure 2). Then, the geoid anomaly $\Delta N^i$ produced by a rectangular prism with a constant density $\rho$ can be expressed analytically in the Cartesian coordinates as [e.g., *Nagy et al.*, 2000]

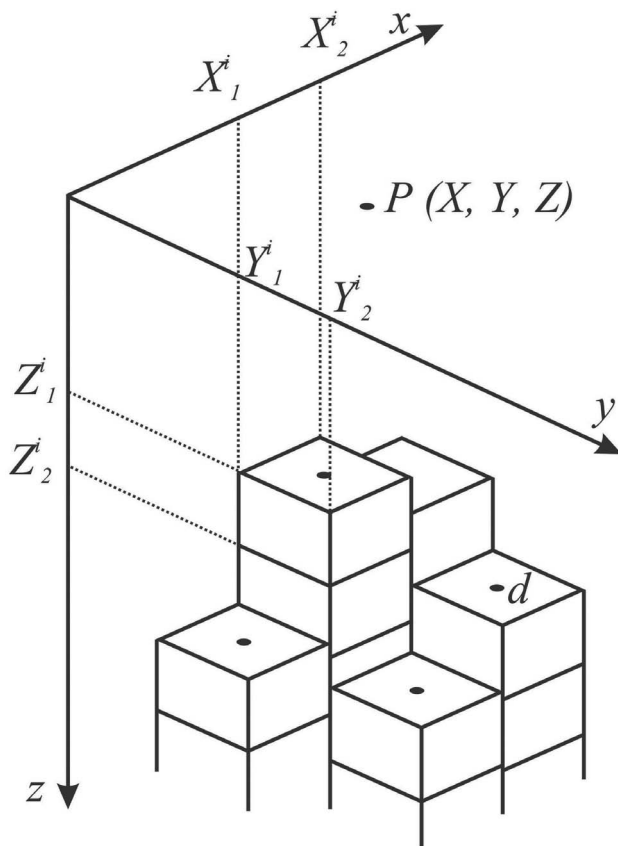$$\Delta N^i(P) = \frac{G\rho}{g} \int_{x_1}^{x_2} \int_{y_1}^{y_2} \int_{z_1}^{z_2} (P-Q)dxdydz, \qquad (2)$$

*Turcotte*, 1978] with constant crustal density. For the oceanic domain, inside and beyond our study area, the model parameters (densities and coordinates of prisms) follow the predictions by the lithospheric cooling models, as described in the following.

[15] The density of oceanic lithosphere is coupled to temperature variations because of thermal contraction, and the density of each prism can be calculated according to the following relation:

$$\rho(z',t) = \rho_m(1 + \alpha(T_m - T(z',t))), \qquad (7)$$

where $\rho_m$ is the density of the mantle at a reference temperature $T_m$, $\alpha$ is the coefficient of thermal expansion, $z'$ is depth measured from the seafloor, and $t$ is age. The temperature structure $T(z', t)$ is dependent on the assumed cooling model. By ignoring the effects of lateral heat conduction, temperature predicted by the half-space cooling model is [e.g., *Turcotte and Schubert*, 2002]

$$T(z',t) = T_m \mathrm{erf}\left(\frac{z'}{2\sqrt{\kappa t}}\right), \qquad (8)$$

where $\kappa$ is thermal diffusivity. For the plate model, the expression for $T(z', t)$ is [e.g., *Turcotte and Schubert*, 2002]

$$T(z',t) = T_m\left[\frac{z'}{H} + \frac{2}{\pi}\sum_{n=1}^{\infty}\frac{1}{n}\exp\left(\frac{-\kappa n^2\pi^2 t}{H^2}\right)\sin\left(\frac{n\pi z'}{H}\right)\right], \quad (9)$$

where $H$ is the asymptotic thermal plate thickness. The values of the thermal parameters used in these model calculations are summarized in Table 1. They are for the half-space model of *Carlson and Johnson* [1994], the plate model of *Parsons and Sclater* [1977] (PSM), and the plate model of *Stein and Stein* [1992] (GDH1). The thickness of the lithosphere predicted by the half-space model is given by [e.g., *Turcotte and Schubert*, 2002]

$$H(t) = 3.64\sqrt{\kappa t}, \qquad (10)$$

which corresponds to the isotherm of $0.99T_m$. For the plate models, the plate thickness $H(t)$ can be found from equation (9) by setting $T(z',t) = T_m$ and solving for $z'$.

[16] As the lithosphere is assumed in local isostatic equilibrium, the integral of density over depth must remain constant as a fracture zone evolves. This compensation is achieved by varying seafloor depth $d(t)$ as

$$d(t) = d_0 + \frac{1}{\rho_m(1 - \alpha T_m) - \rho_w}\int_0^H \Delta\rho(z,t)dz, \qquad (11)$$



**Figure 2.** Schematic diagram showing the discretization of a model lithosphere into an array of rectangular prisms; $d$ is the seafloor depth.

where

$$P = xy\ln(z + r) + yz\ln(x + r) + xy\ln(y + r), \qquad (3)$$

$$Q = \frac{z^2}{2}\arctan\left(\frac{xy}{zr}\right) + \frac{x^2}{2}\arctan\left(\frac{yz}{xr}\right) + \frac{y^2}{2}\arctan\left(\frac{xz}{yr}\right), \qquad (4)$$

$$x_j = X_j^i - X_P, y_j = Y_j^i - Y_P, z_j = Z_j^i - Z_P, \qquad (5)$$

$$r = \sqrt{x^2 + y^2 + z^2}, \qquad (6)$$

$G$ is the gravitational constant, and $g$ is the mean surface gravity. The contribution of all prisms at the point $P$ will be the sum: $N(P) = \sum_{i=1}^{n}\Delta N^i(P)$, where $n$ is the total number of prisms. To avoid edge effects, the model has to be extended far beyond the limits of the study area [e.g., *Ayala et al.*, 1996]. In this study we choose to extend the area of computation laterally by 50% in all directions. For continental areas, we simply assume the topography to be isostatically balanced by Moho depth variations in relation to a reference depth, which was set to 40 km. The coordinates of the top and bottom of the prisms are then inferred from, respectively, the surface topography and the thickness of crustal root according to Airy compensation [*Haxby and*

**Table 1.** Thermal Parameters Used in Geoid Calculations

|  | HSC | GDH1 | PSM |
|---|---|---|---|
| Mantle density $\rho_m$ (kg.m$^{-3}$) | 3300 | 3300 | 3300 |
| Water density $\rho_w$ (kg.m$^{-3}$) | 1000 | 1000 | 1000 |
| Temperature $T_m$ (K) | 1335 | 1450 | 1350 |
| Thermal expansion $\alpha$ (K$^{-1}$) | $3.1 \times 10^{-5}$ | $3.1 \times 10^{-5}$ | $3.1 \times 10^{-5}$ |
| Thermal diffusivity K (m$^2$.s$^{-1}$) | $8 \times 10^{-7}$ | $8 \times 10^{-7}$ | $8 \times 10^{-7}$ |
| Asymptotic plate thickness H (km) |  | 95 | 125 |

where $d_0$ is the zero-age seafloor depth and $\rho_w$ is the density of seawater.

## 4. Application to Mendocino Fracture Zone

### 4.1. Location and Data

[17] We apply the wavelet approach on the Mendocino Fracture Zone. As shown in Figure 3a, this fracture zone runs continuously from the west coast of North America at ~40°N to Hess Rise, which is located at the bend of the Hawaii-Emperor seamount chain. The Mendocino Fracture Zone has relatively simple topographic expressions to the east of 150°W, but the western part is more diffuse and constitutes a wide, topographically complex zone [*Mammerickx and Smith*, 1981]. We thus consider only the younger part (ages < 60 Ma) of this fracture zone, extending from 150°W to 127°W (see the black box of Figure 3a). As the geoid slope-age relation predicted by cooling models begins to differ at about 40 Ma [e.g., *Sandwell*, 1984], we should still be able to discriminate between different models in this area. The Mendocino Fracture Zone was chosen because of its large age offset of 25–30 Ma [*Menard and Atwater*, 1968], and for this reason, it has been the subject of a number of investigations in the past [e.g., *Detrick*, 1981; *Cazenave et al.*, 1982; *Sandwell and Schubert*, 1982; *Richardson et al.*, 1995], thereby being an optimal place to test our new wavelet-based approach. Moreover, the Pioneer Fracture Zone, with age offset of 3–5 Ma, lies approximately 150 km to the south of the portion. This superposition of structures allows us to test the ability of the wavelet analysis to separate their signatures in the geoid.

[18] In this study, we analyze high-resolution geoid data from the GRACE mission measurements [*Tapley et al.*, 2004]. We use geoid anomalies derived from the global spherical harmonics model EIGEN-GL04C [*Förste et al.*, 2008], which is a combination of GRACE and altimeter-derived gravity data (Figure 3b). It is complete up to degree and order 360 in terms of spherical harmonic coefficients and thus resolves geoid anomalies at wavelengths down to 55 km. Seafloor ages are taken from *Müller et al.* [2008] (Figure 3c).

### 4.2. The Total Geoid Step

[19] Geoid anomalies for a subsiding, thermally compensated oceanic lithosphere as predicted by the half-space model (HSC) and plate models (GDH1 and PSM) are shown in Figure 4. Results with lateral density variations are shown on the right side, and those from the usual analytical solutions on the left side [*Haxby and Turcotte*, 1978; *Sandwell and Schubert*, 1980; *Parsons and Richter*, 1980]. The observed and synthetic geoids along three different profiles (corresponding to ages of 20, 40 and 50 Ma) crossing the Mendocino Fracture Zone are shown in Figure 5. Including lateral density variations, the geoid step predicted by the half-space cooling model becomes smoother across the FZ and fits the data significantly better. This is especially true for ages greater than 20 Ma. A similar comment may be made for the geoid anomalies calculated for the PSM plate model. Regarding the GDH1 plate model, the theoretical geoid offsets calculated with lateral density variations do not differ much from those predicted by the classical approximations [*Sandwell and Schubert*, 1980; *Parsons and Richter*, 1980].

[20] Although a geoid step associated with the Mendocino Fracture Zone can clearly be recognized in the data, it seems difficult to delimitate precisely the portion of the signal related to lithosphere cooling. On all profiles the observed geoid height increases from south to north, much more than predicted by any of cooling models. This regional trend is probably due to deep density variations in the mantle unrelated to the thermal structure of the lithosphere and constitutes an important source of error in the offset determination [e.g., *Detrick*, 1981]. Moreover, an additional geoid step is visible about 150–200 km south of the Mendocino Fracture Zone (around latitude 38.5°N). This signal, associated with the Pioneer Fracture Zone, can complicate the interpretation of the geoid signature of the Mendocino FZ. In order to isolate the geoid signal of the lithospheric thermal structure located below the Mendocino FZ, we apply a continuous wavelet transform, at scales ranging between 100 and 500 km, on the data as well as on the predictions calculated numerically with lateral density variations.

### 4.3. The Localized Geoid Step

[21] The geoid component associated with the age contrast may be identified by comparing the observed geoid data with model predictions, the latter of which depend only on the thermal structure of the lithosphere, in the wavelet transform domain. Figure 6 shows that a best agreement is obtained at 100 km scale. At this scale, the geoid signal provides an integrated view of Earth masses down to a depth of about 100 km, so it is indeed expected to be sensitive mainly to the density structure of the lithosphere. Results of the continuous wavelet transform at scale of 100 km are shown in Figure 7. For comparison, we also show results obtained at 200 km in Figure 8. At 100 km scale, the wavelet transform reveals two distinct positive peaks in the data, corresponding to the geoid signatures of the Mendocino FZ (latitude 40°N) and the Pioneer FZ (latitude 38.5°N). The localized geoid step associated with the Pioneer FZ does not exceed 0.2 m and seems to disappear after 40 Ma. A decrease of the localized geoid step is also observed along the Mendocino FZ, varying from 1.6 m at 20 Ma to 1 m at 50 Ma. At 200 km scale, the signal is smoother. The geoid signature related to the Pioneer FZ becomes more difficult to identify and affects the signal of the Mendocino FZ. The scale of 100 km is thus preferred also on the basis of the particular geographical setting of this fracture zone. Consequently, we only discuss the results obtained at this scale in the following.

[22] As the observed and theoretical geoid offsets are localized in the same manner, we can directly compare them. The three cooling models give very close results, and only the GDH1 plate model differs at 50 Ma (Figure 7). At 20 Ma, the analyzed geoid offset predicted by the GDH1 model is also slightly greater than those derived from the half-space and the PSM models. This is simply because of different thermal parameters used in geoid calculations. The observed and calculated geoid steps across the Mendocino FZ share a very similar shape after the wavelet transform, indicating that our wavelet approach is able to isolate the fracture-zone geoid signature from regional contributions. The amplitude of the synthetic geoid offset is, however, weaker at 20 and 40 Ma. These discrepancies will be discussed in the next sections.
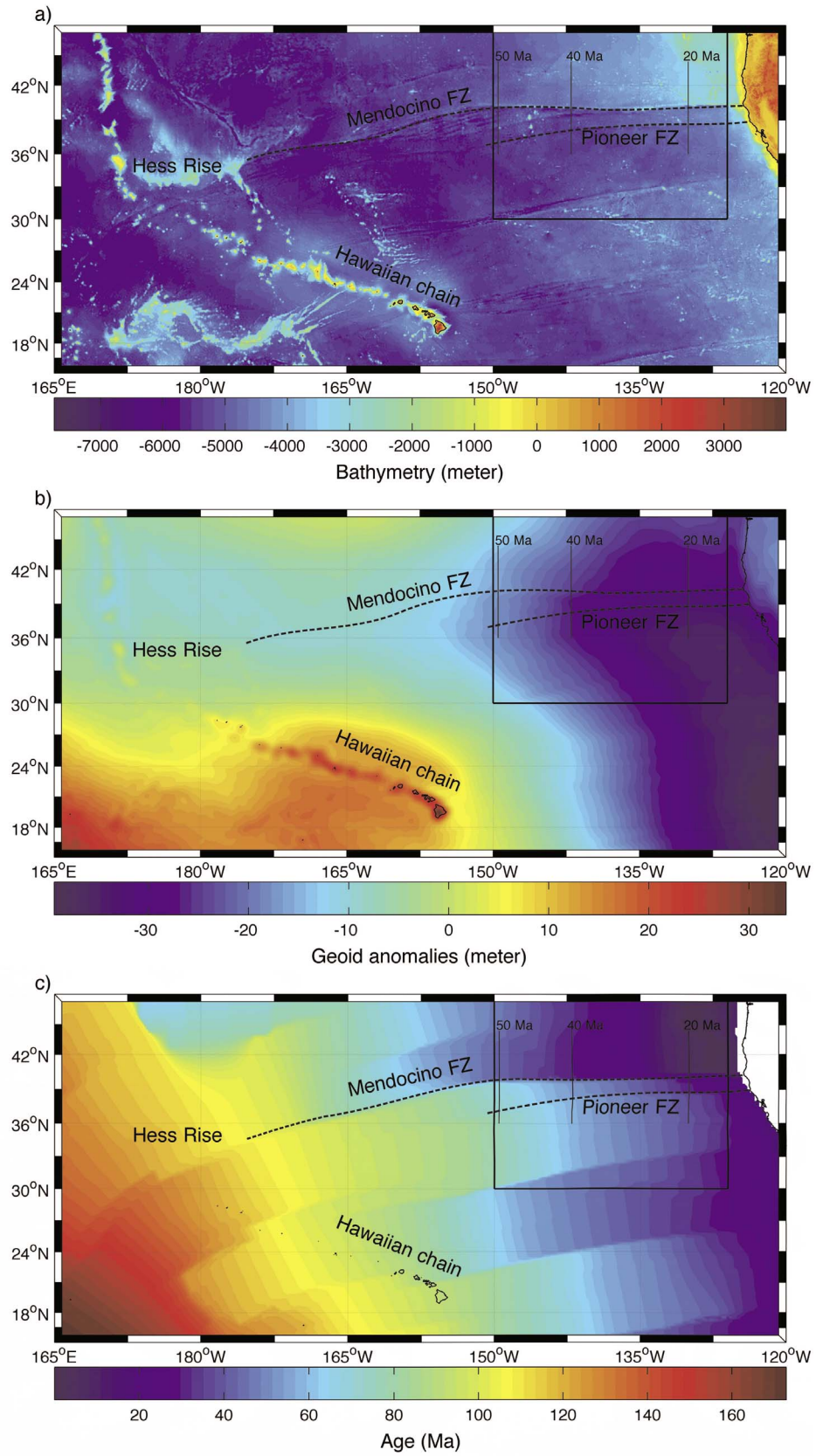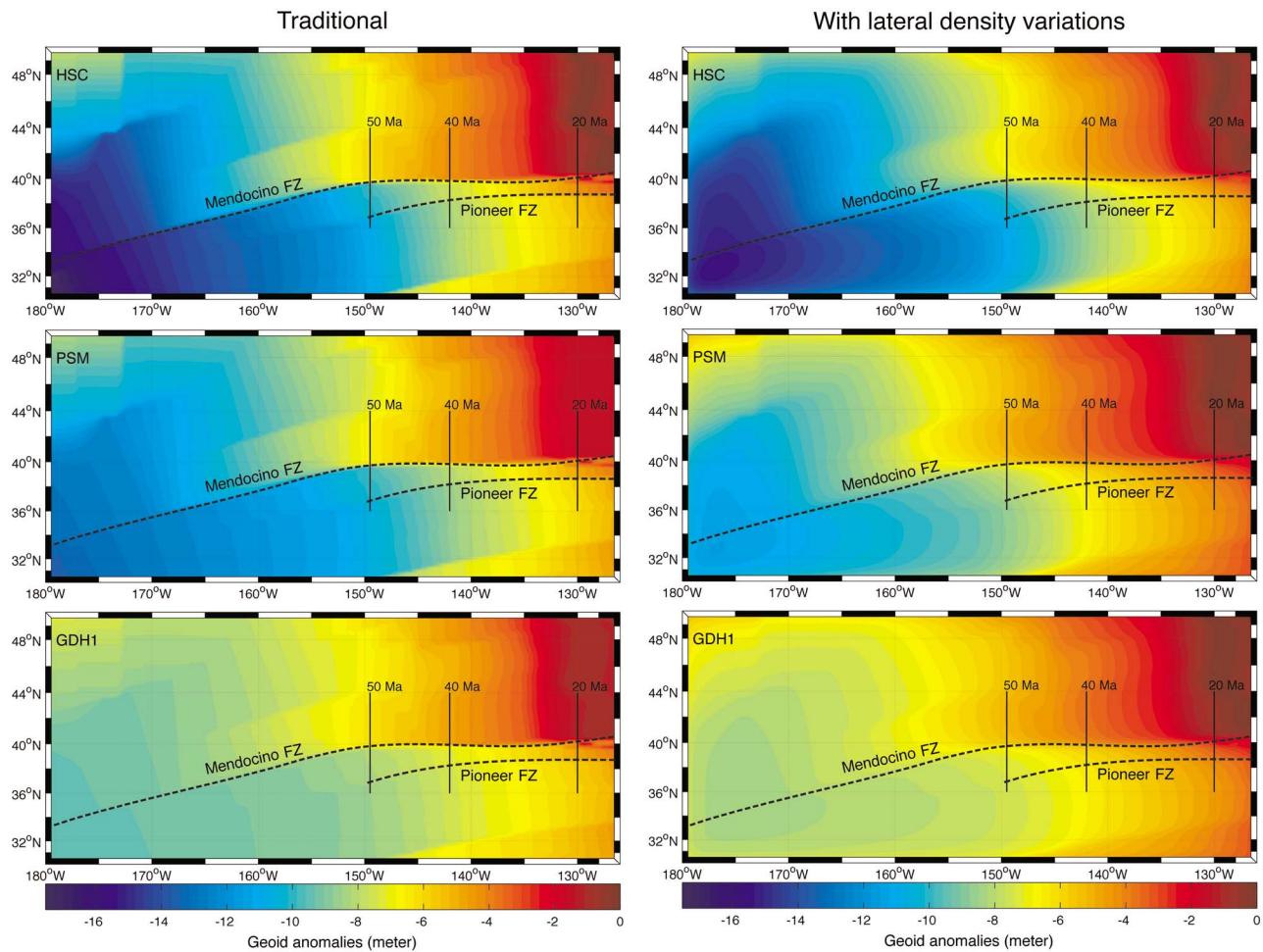
**Figure 3**

**Figure 4.** Geoid anomalies calculated from (top) the half-space cooling (HSC) model, (middle) the PSM plate model, and (bottom) the GDH1 plate model. The results obtained in this study by considering lateral density variations are shown on the right side whereas the predictions derived from the usual analytical solutions are represented on the left side.

### 4.4. The Geoid Slope-Age Relationship at 100 km Scale

[23] The geoid slopes as a function of the mean age of the two sides of the fracture zone are plotted in Figure 9. The geoid-slope data along the Mendocino FZ is in general compatible with the predictions of thermal models derived from this study, contrary to the conclusion of previous studies based on the traditional analytical solutions [e.g., *Cazenave*, 1984; *Driscoll and Parsons*, 1988; *Marty and Cazenave*, 1988]. Two notable misfits are, however, observed for ages younger than 20 Ma and for ages between 32 and 42 Ma. The first, already reported in the previous studies [e.g., *Marty and Cazenave*, 1988; *Wessel and Haxby*, 1989; *Richardson et al.*, 1995], has been attributed to small-scale convection driven by the horizontal temperature gradients beneath the fracture zone [e.g., *Robinson et al.*, 1988]. However, in the geodynamic models, such small-scale convection occurs typically at spatial scales that are larger than 100 km, and is thus probably inadequate to explain this discrepancy. At this scale, deviations from the theoretical trend could be related to hydrothermal flow when the seafloor is young enough, or to some intrinsic geological variabilities. Further studies are necessary to better identify the causes of these discrepancies. Moreover, uncertainties in the crustal ages would directly contribute to the observed scatter.

[24] As already mentioned, small changes in the thermal structure near the base of the lithosphere are expected to produce changes in the geoid slope. Theoretical geoid slope-age

**Figure 3.** (a) Predicted bathymetry in the Northeast Pacific [*Smith and Sandwell*, 1997]. The Mendocino Fracture Zone is located at 40°N and runs from the west coast of North America to the Hess Rise located near the bend of the Hawaii-Emperor seamount chain. The Pioneer Fracture Zone is about 150 km south of the youngest portion of the Mendocino FZ. The black box represents the study area. (b) The EIGEN-GL04C geoid model up to spherical harmonics degree and order 360 [*Förste et al.*, 2008]. (c) Seafloor age [*Müller et al.*, 2008].
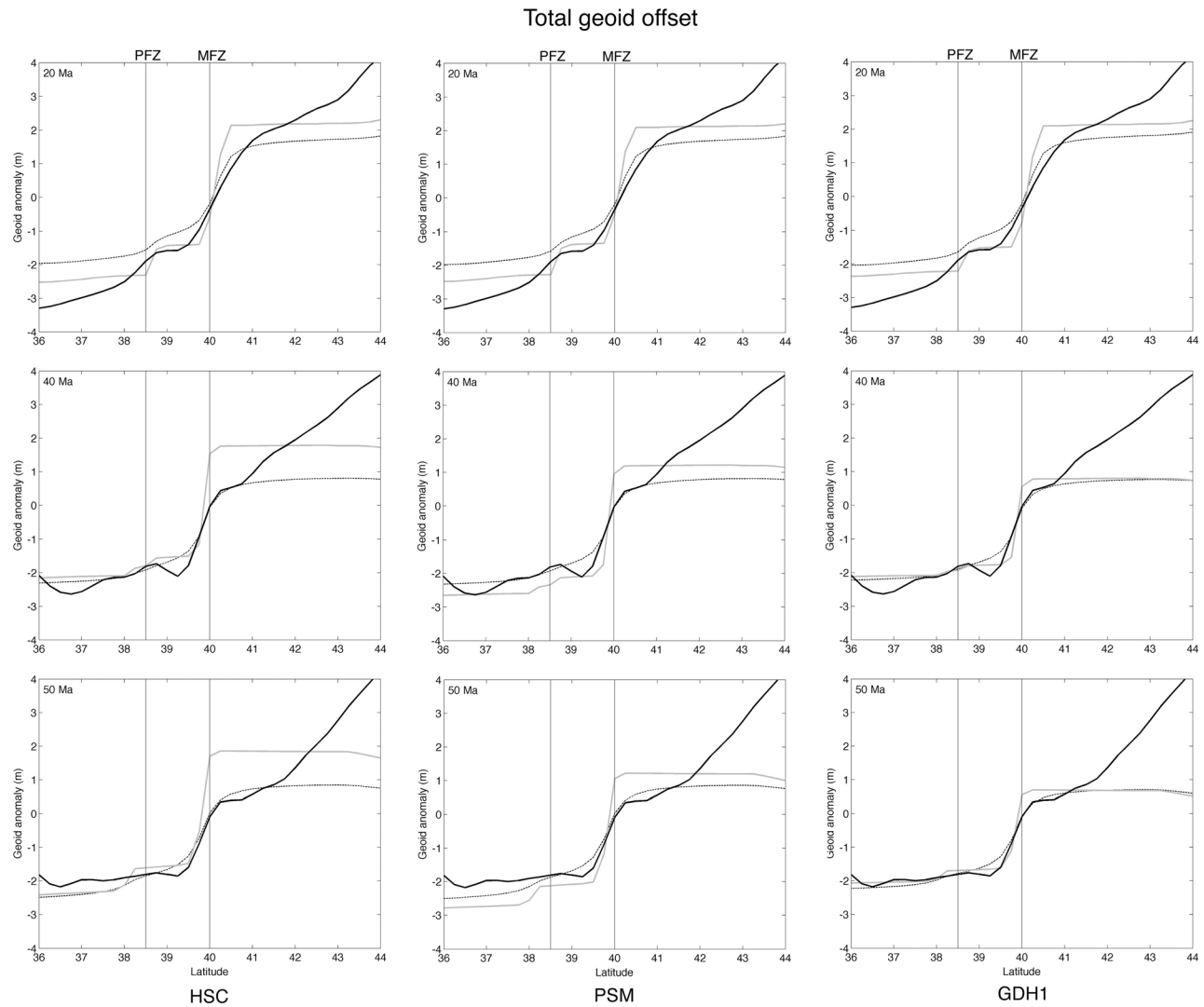
Total geoid offset



**Figure 5.** The observed (solid black line) and theoretical geoid offset (solid gray and dashed dark lines) across the Mendocino Fracture Zone at ages of (top) 20, (middle) 40 and (bottom) 50 Ma. The dark dashed line represents the synthetic geoid step obtained in this study; the gray line is derived from the analytical expressions.

relations indeed differ at ages greater than 40 Ma (Figure 9). Such difference is, however, too small when lateral density variations are properly taken into account, and all of the three cooling models similarly fit the data.

## 5. Discussion

[25] The wavelet approach allows us, for the first time, to properly extract the geoid signal associated with the Mendocino Fracture Zone. This is owing to the ability of the chosen wavelet to efficiently reduce the unwanted regional contributions, which could otherwise significantly bias the estimate of the geoid offset. A common method to estimate a geoid step consists of fitting a low-order polynomial over a profile to approximate a regional geoid field, and then fitting a step function across a fracture zone to estimate its geoid offset due to differential cooling. In order to avoid biasing the estimate of such a regional component by local effects

associated with lateral heat conduction [*Louden and Forsyth*, 1976], flexural deformation [*Sandwell*, 1984], and thermal stresses [*Parmentier and Haxby*, 1986], data within 100–200 km of a fracture zone are usually ignored. The width of such an exclusion window is, however, directly related to the estimate of a geoid offset. According to *Sandwell* [1984], if the window is too small, the true geoid step will be underestimated by as much as 50%. Ironically, it is only in the immediate vicinity of a fracture zone that the geoid signature of differential lithosphere cooling can be unambiguously identified. Furthermore, the more observations one excludes, the harder it is to separate a geoid step from any regional trend. This underlines the importance of our wavelet approach, which allows us to naturally localize the signature associated with a fracture zone in the total geoid, without using a rather ad hoc exclusion window.

[26] As lateral heat conduction, differential subsidence, and thermal bending stresses are commonly discussed as
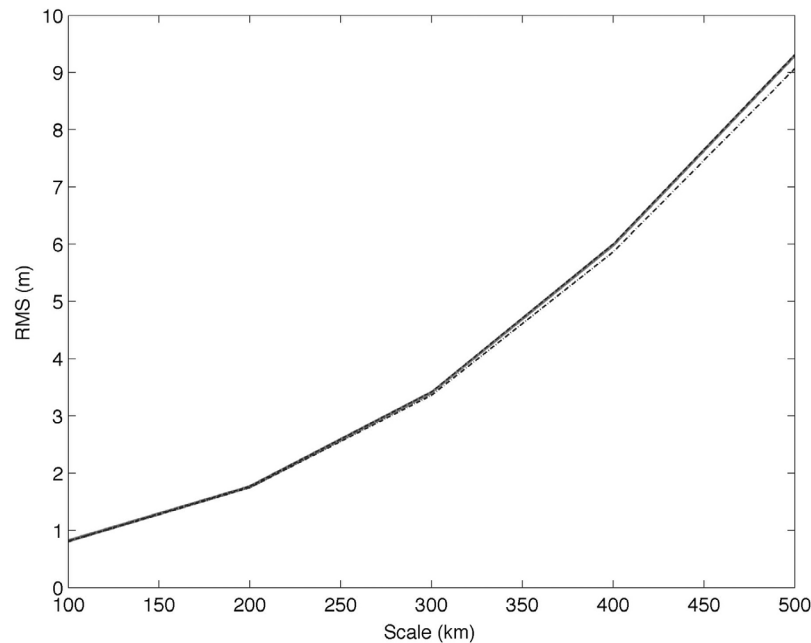
**Figure 6.** Root-mean square (RMS) difference between the synthetic geoid offset, as predicted from cooling models considering lateral density variations, and the observed geoid offset, at each scale of the wavelet analysis. Here RMS values are based on geoid profiles across the Mendocino Fracture Zone at 40 Ma (as shown in Figures 7 and 8, at 100 and 200 km scales, respectively). RMS values for the half-space, GDH1, and PSM models are shown by, respectively, gray, dash-dot, and dashed lines.

processes occurring at short-wavelengths, it would be interesting to estimate their potential contributions to our geoid analysis at 100 km scale and see whether they could explain or not part of the discrepancies between the observed and synthetic geoid offsets. Several studies take account for these effects in order to improve the estimate of geoid offsets [e.g., *Louden and Forsyth*, 1976; *Detrick*, 1981; *Sandwell*, 1984; *Parmentier and Haxby*, 1986; *Marty and Cazenave*, 1988; *Wessel and Haxby*, 1989]. Assuming local isostatic equilibrium, previous studies show that lateral heat conduction tends to smooth a geoid step [*Louden and Forsyth*, 1976; *Detrick*, 1981; *Sandwell*, 1984]. At 100 km scale, the amplitude of the observed geoid offset is, however, greater than that of the synthetic offset. Thus, this smoothing effect cannot explain the observed discrepancy, and we may further infer that such smoothing effect could be insignificant. Differential subsidence between the two sides of the fault (the younger side cools more rapidly than the older side) could deflect an elastic lithosphere, producing in the topography a ridge on the younger side, and a trough on the older side [*Sandwell and Schubert*, 1982]. This flexural topography, however, should intensify and become more rugged with increasing age, thereby failing to explain the observed geoid misfits, which are most pronounced at young ages. Finally, according to *Parmentier and Haxby* [1986], thermal stresses can also produce an additional flexural topography that could give rise to a distinctive geoid

signature. However, a recent study on thermal stresses in oceanic lithosphere shows that, given the strength of silicate rocks, thermal stresses are most likely to be released by thermal cracks [*Korenaga*, 2007], so their possible contributions to topographic deformations are expected to be much reduced than previously thought, though this issue needs to be better quantified in future.

[27] As the theoretical geoid anomalies derived from our cooling models can explain the observed geoid reasonably well, we may conclude that the geoid anomaly localized at 100 km scale across the Mendocino Fracture Zone reflects lithosphere cooling. Furthermore, we show that more realistic density distributions across the fracture zone can considerably change the interpretation of results. Including both the effects of vertical and lateral density variations, the predictions from the half-space model and the plate models differ not as much as expected from the classical analytical solutions. Accordingly, a satisfactory agreement is obtained between the observed and synthetic geoid slope-age relationship for all of three different cooling models. The half-space cooling, usually ruled out in favor of the plate model by the previous studies, can remain as a certain possibility.

[28] However, at this point, our results do not allow us to discriminate between the different cooling models. To resolve this issue, it is thus necessary to conduct a parameter-space search to estimate the best fit cooling model. Furthermore, a global wavelet analysis of geoid anomalies

**Figure 7.** Localized geoid offsets across the Mendocino Fracture Zone at 100 km scale. The observed geoid step is shown at (top) 20, (middle) 40 and (bottom) 50 Ma by thick black line, whereas the synthetic geoids predicted from the half-space, GDH1, and PSM models are shown by, respectively, solid gray, dash-dot, and dashed lines.
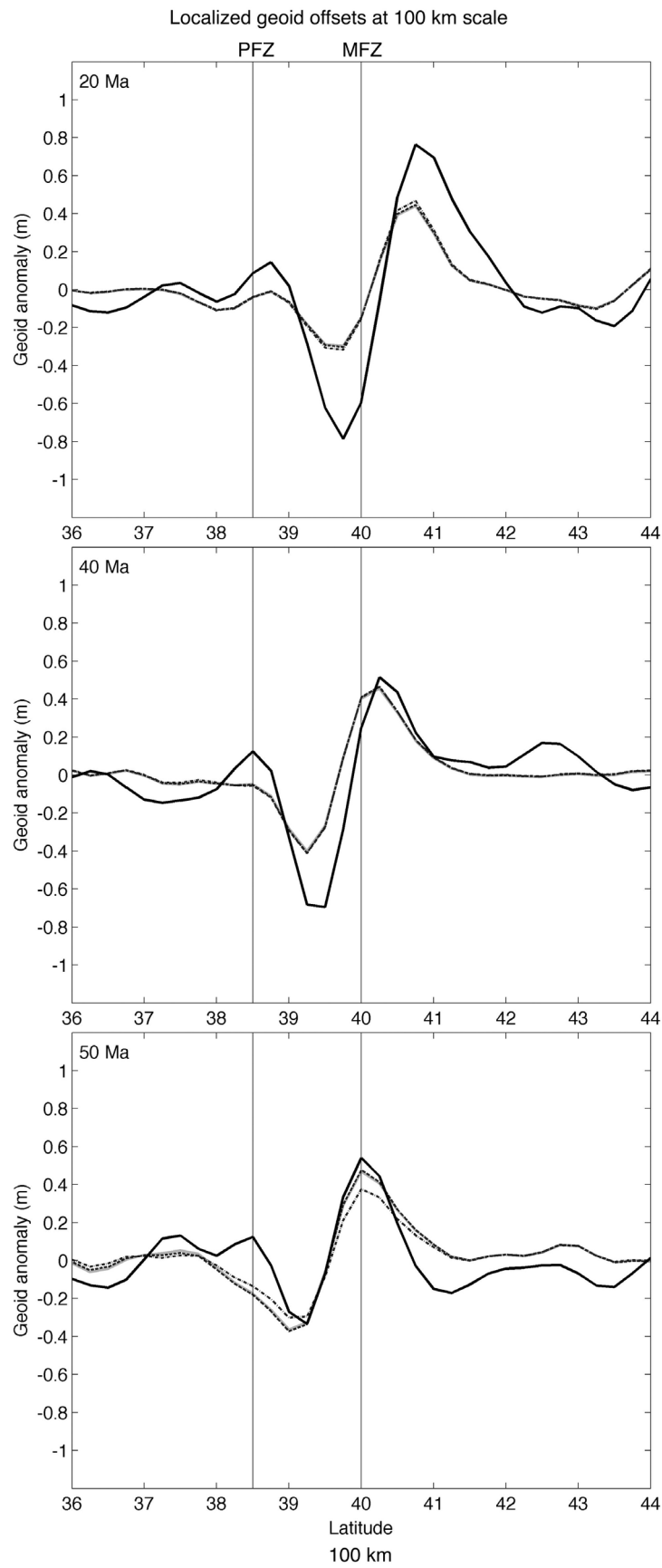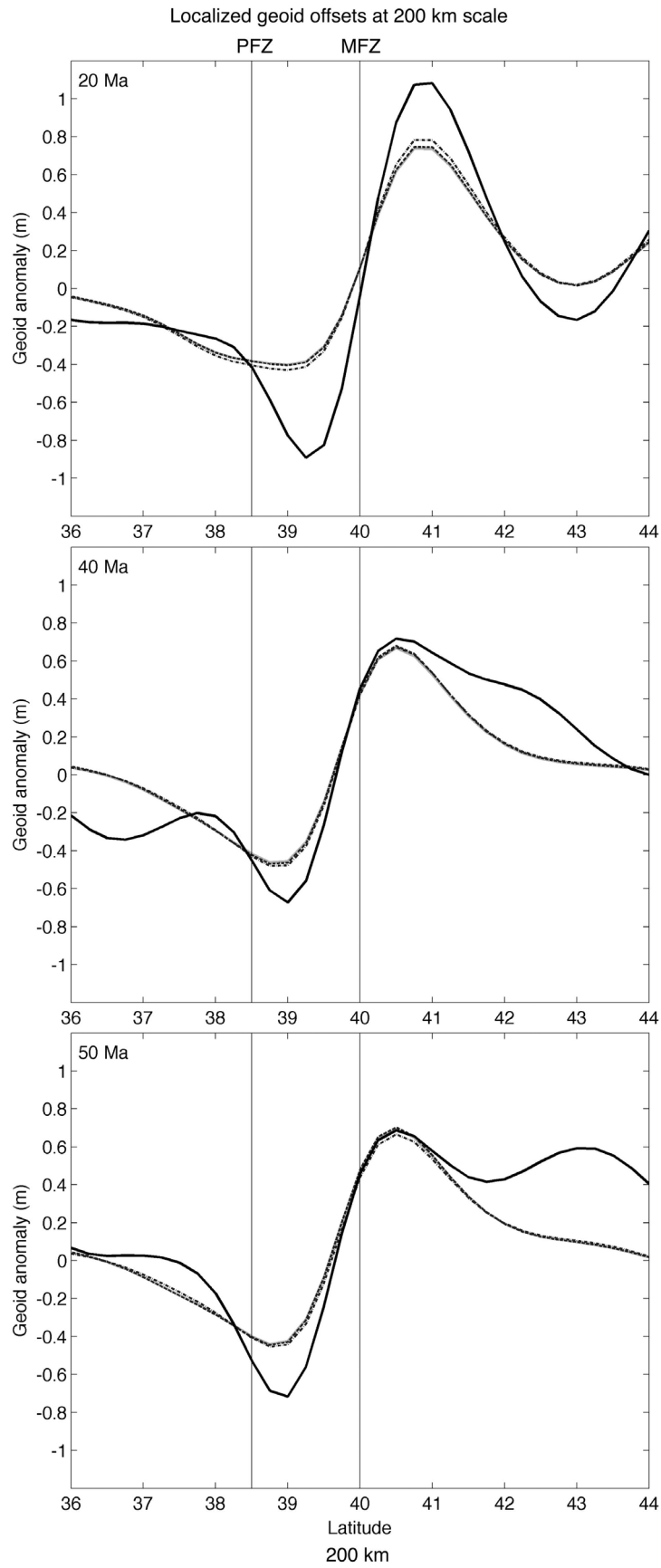
Localized geoid offsets at 100 km scale



**Figure 7**

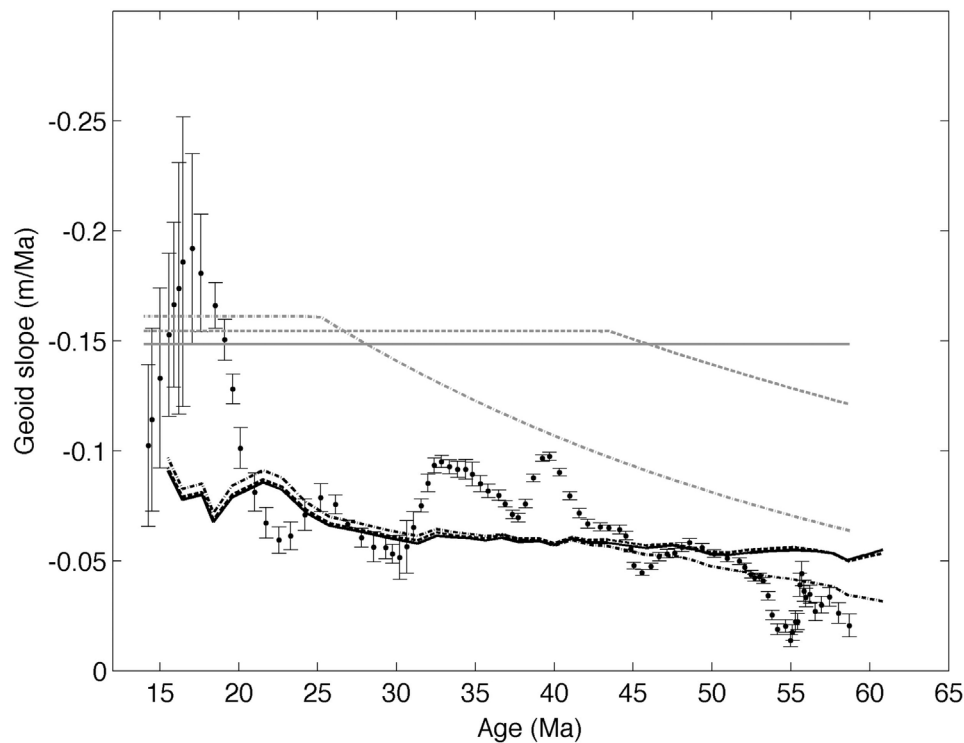**Figure 8.** Same as Figure 7, but at 200 km scale.

**Figure 9.** Geoid-slope data (black dots) across the Mendocino Fracture Zone compared to predictions of thermal models (solid black: half-space model, dash-dot: GDH1 model, and dashed: PSM model) based on 100-km-scale wavelet analysis. Classical predictions are shown as gray lines (solid: HSC model, dash-dot: GDH1 model, and dashed: PSM model). Error bars denote uncertainties due to crustal age and geoid data.

across fracture zones will allow us to determine if our results are specific to the Mendocino Fracture Zone or not. The examination of four other Pacific fracture zones [*Wessel and Haxby*, 1989] also evidence an agreement between existing conductive models and observations. Extending the analysis to the Atlantic Ocean, however, *Marty and Cazenave* [1988] report that in most cases the geoid slope-age relationship presents a complex behavior and argue for contribution from a dynamic mechanism such as small-scale convection. In that case, the wavelet method will permit to better identify these additional mechanisms occurring beneath fracture zones. Finally, by comparing with theoretical expectation for lithospheric cooling in the wavelet transform domain, we can successfully identify unusual signals, which may allow us to constrain the fine-scale density structure of oceanic lithosphere. It will be interesting to implement a new inversion scheme that can exploit such hitherto-overlooked local anomalies.

## 6. Conclusion

[29] In order to improve our understanding of the thermal evolution of oceanic lithosphere, we apply a continuous wavelet transform to the geoid along the Mendocino Fracture Zone. This analysis allows us to accurately estimate geoid offsets across the fracture zone and to define a new geoid slope-age relationship. The comparison of the observed geoid offsets with those predicted from three cooling models shows that our approach can remove unwanted regional contributions and isolate the geoid signature due to

lithosphere cooling. This investigation suggests that all of standard cooling models are in general agreement with the estimates of geoid slopes measured at the Mendocino Fracture zone. However, future studies are needed to discriminate between different cooling models, and to better understand the causes of small-scale geoid anomalies detected along the fracture zone, which may hold important information on the evolution of oceanic lithosphere.

## References

Ayala, C., M. Fernandez, M. Torne, and J. Pous (1996), Two-dimensional geoid modeling: Some remarks on Chapman's algorithm, *Geophys. J. Int.*, *127*, 542–544, doi:10.1111/j.1365-246X.1996.tb04739.x.

Cadio, C., I. Panet, A. Davaille, M. Diament, L. Métivier, and O. de Viron (2011), Pacific geoid anomalies revisited in light of thermochemical oscillating domes in the lower mantle, *Earth Planet. Sci. Lett.*, *306*, 123–135, doi:10.1016/j.epsl.2011.03.040.

Cadio, C., M. Ballmer, I. Panet, N. Ribe, and M. Diament (2012), New constraints on the origin of the Hawaiian swell from wavelet analysis of the geoid to topography ratio, *Earth Planet. Sci. Lett.*, in press.

Carlson, R. L., and H. P. Johnson (1994), On modeling the thermal evolution of the oceanic upper mantle: An assessment of the cooling plate model, *J. Geophys. Res.*, *99*, 3201–3214, doi:10.1029/93JB02696.

Cazenave, A. (1984), Thermal cooling of the oceanic lithosphere: New constraints from geoid height data, *Earth Planet. Sci. Lett.*, *70*, 395–406, doi:10.1016/0012-821X(84)90023-2.

Cazenave, A., B. Lago, and K. Dominh (1982), Geoid anomalies over the Northeast Pacific fracture zones from satellite altimeter data, *Geophys. J. R. Astron. Soc.*, *69*, 15–31, doi:10.1111/j.1365-246X.1982.tb04932.x.

Chambodut, A., I. Panet, M. Mandea, M. Diament, M. Holschneider, and O. Jamet (2005), Wavelet frames: An alternative to spherical harmonic

representation of potential fields, *Geophys. J. Int.*, *163*(3), 875–899, doi:10.1111/j.1365-246X.2005.02754.x.

Crough, S. T. (1977), Approximate solutions for the formation of the lithosphere, *Phys. Earth Planet. Inter.*, *14*, 365–377, doi:10.1016/0031-9201(77)90169-8.

Crough, S. T. (1979), Geoid anomalies across fracture zones and the thickness of the lithosphere, *Earth Planet. Sci. Lett.*, *44*, 224–230, doi:10.1016/0012-821X(79)90170-5.

Davies, G. F. (1988), Ocean bathymetry and mantle convection 2: Small-scale floor, *J. Geophys. Res.*, *93*, 10,481–10,488, doi:10.1029/JB093iB09p10481.

Davies, G. F., and F. Pribac (1993), Mesozoic seafloor subsidence and the Darwin Rise, past and present, in *The Mesozoic Pacific: Geology, Tectonics, and Volcanism: A Volume in Memory of Sy Schlanger*, *Geophys. Monogr. Ser.*, vol. 77, edited by M. S. Pringle et al., pp. 39–52, AGU, Washington, D. C., doi:10.1029/GM077p0039.

Davis, E. E., and C. R. B. Lister (1974), Fundamentals of ridge crest topography, *Earth Planet. Sci. Lett.*, *21*, 405–413, doi:10.1016/0012-821X(74)90180-0.

Detrick, R. S. (1981), An analysis of geoid anomalies across the Mendocino fracture zone: Implications for thermal models of the lithosphere, *J. Geophys. Res.*, *86*, 11,751–11,762, doi:10.1029/JB086iB12p11751.

Driscoll, M. L., and B. Parsons (1988), Cooling of the oceanic lithosphere–evidence from geoid anomalies across the Udintsev and Eltanin fracture zones, *Earth Planet. Sci. Lett.*, *88*, 289–307, doi:10.1016/0012-821X(88)90086-6.

Förste, C., et al. (2008), The GeoForschungsZentrum Potsdam/Groupe de Recherche de Géodésie Spatiale satellite-only and combined gravity field models: EIGEN-GL04S1 and EIGEN-GL04C, *J. Geod.*, *82*, 331–346, doi:10.1007/s00190-007-0183-8.

Forsyth, D. W. (1977), The evolution of the upper mantle beneath mid-ocean ridges, *Tectonophysics*, *38*, 89–118, doi:10.1016/0040-1951(77)90202-5.

Hager, B. H. (1978), Oceanic plate motions driven by lithospheric thickening and subducted slabs, *Nature*, *276*, 156–159, doi:10.1038/276156a0.

Haxby, W. F., and D. L. Turcotte (1978), On isostatic geoid anomalies, *J. Geophys. Res.*, *83*(B11), 5473–5478, doi:10.1029/JB083iB11p05473.

Heestand, R. L., and S. T. Crough (1981), The effect of hot spots on the oceanic age-depth relation, *J. Geophys. Res.*, *86*(B7), 6107–6114, doi:10.1029/JB086iB07p06107.

Holschneider, M. (1995), *Wavelets: An Analysis Tool*, Oxford Sci., Oxford, U. K.

Holschneider, M., A. Chambodut, and M. Mandea (2003), From global to regional analysis of the magnetic field on the sphere using wavelet frames, *Phys. Earth Planet. Inter.*, *135*, 107–124, doi:10.1016/S0031-9201(02)00210-8.

Korenaga, J. (2007), Thermal cracking and the deep hydration of oceanic lithosphere: A key to the generation of plate tectonics?, *J. Geophys. Res.*, *112*, B05408, doi:10.1029/2006JB004502.

Korenaga, T., and J. Korenaga (2008), Subsidence of normal oceanic lithosphere, apparent thermal expansivity, and seafloor flattening, *Earth Planet. Sci. Lett.*, *268*, 41–51, doi:10.1016/j.epsl.2007.12.022.

Langseth, M. G., X. Le Pichon, and M. Ewing (1966), Crustal structure of mid-ocean ridges: 5 Heat flow through the Atlantic Ocean floor and convection currents, *J. Geophys. Res.*, *71*(5), 321–325, 355.

Louden, K. E., and D. W. Forsyth (1976), Thermal conduction across fracture zones and the gravitational edge effect, *J. Geophys. Res.*, *81*(26), 4869–4874, doi:10.1029/JB081i026p04869.

Mammerickx, J., and S. W. Smith (1981), *Bathymetry of the Northeast Pacific*, Geol. Soc. of Am., Boulder, Colo.

Marty, J.-C., and A. Cazenave (1988), Thermal evolution of the lithosphere beneath fracture zones inferred from geoid anomalies, *Geophys. Res. Lett.*, *15*, 593–596, doi:10.1029/GL015i006p00593.

McKenzie, D. P. (1967), Some remarks on heat flow and gravity anomalies, *J. Geophys. Res.*, *72*(6), 261–266, 273.

Menard, H. W., and T. M. Atwater (1968), Changes in direction of seafloor spreading, *Nature*, *219*, 463–467, doi:10.1038/219463a0.

Müller, R. D., M. Sdrolias, C. Gaina, and W. R. Roest (2008), Age, spreading rates, and spreading asymmetry of the world's ocean crust, *Geochem. Geophys. Geosyst.*, *9*, Q04006, doi:10.1029/2007GC001743.

Nagy, D., G. Papp, and J. Benedek (2000), The gravitational potential and its derivatives for the prism, *J. Geod.*, *74*, 552–560, doi:10.1007/s001900000116.

Ockendon, J. R., and D. L. Turcotte (1977), On the gravitational potential and field anomalies due to thin mass layers, *Geophys. J.*, *48*, 479–492, doi:10.1111/j.1365-246X.1977.tb03684.x.

Panet, I., A. Chambodut, M. Diament, M. Holschneider, and O. Jamet (2006), New insights on intraplate volcanism in French Polynesia from wavelet analysis of GRACE, CHAMP, and sea surface data, *J. Geophys. Res.*, *111*, B09403, doi:10.1029/2005JB004141.

Panet, I., V. Mikhailo, M. Diament, F. Pollitz, G. King, O. de Viron, M. Holschneider, R. Biancale, and J.-M. Lemoine (2007), Co-seismic and post-seismic signatures of the Sumatra December 2004 and March 2005 earthquakes in GRACE satellite gravity, *Geophys. J. Int.*, *171*, 177–190, doi:10.1111/j.1365-246X.2007.03525.x.

Parker, R. L., and D. W. Oldenburg (1973), Thermal model of ocean ridges, *Nature Phys. Sci.*, *242*, 137–139.

Parmentier, E. M., and W. F. Haxby (1986), Thermal stresses in the oceanic lithosphere: Evidence from geoid anomalies at fracture zones, *J. Geophys. Res.*, *91*(B7), 7193–7204, doi:10.1029/JB091iB07p07193.

Parsons, B., and D. McKenzie (1978), Mantle convection and the thermal structure of the plates, *J. Geophys. Res.*, *83*(B9), 4485–4496, doi:10.1029/JB083iB09p04485.

Parsons, B., and F. M. Richter (1980), A relation between driving forces and geoid anomaly associated with mid-ocean ridges, *Earth Planet. Sci. Lett.*, *51*, 445–450, doi:10.1016/0012-821X(80)90223-X.

Parsons, B., and J. G. Sclater (1977), An analysis of the variation of ocean floor bathymetry and heat flow with age, *J. Geophys. Res.*, *82*, 803–827, doi:10.1029/JB082i005p00803.

Phipps Morgan, J., and W. H. F. Smith (1992), Flattening of the sea floor as a response to asthenospheric flow, *Nature*, *359*, 524–527, doi:10.1038/359524a0.

Richardson, W. P., S. Stein, C. A. Stein, and M. T. Zuber (1995), Geoid data and thermal structure of the oceanic lithosphere, *Geophys. Res. Lett.*, *22*(14), 1913–1916, doi:10.1029/95GL01595.

Richter, F. M., and B. Parsons (1975), On the interaction of two scales of convection in the mantle, *J. Geophys. Res.*, *80*(17), 2529–2541, doi:10.1029/JB080i017p02529.

Robinson, E. M., B. Parsons, and M. Driscoll (1988), The effect of a shallow low-viscosity zone on the mantle flow, the geoid anomalies and geoid and depth-age relationships at fracture zones, *Geophys. J.*, *93*, 25–43, doi:10.1111/j.1365-246X.1988.tb01386.x.

Sandwell, D. T. (1984), Thermomechanical evolution of oceanic fracture zones, *J. Geophys. Res.*, *89*, 11,401–11,413, doi:10.1029/JB089iB13p11401.

Sandwell, D., and G. Schubert (1980), Geoid Height Versus Age for Symmetric Spreading Ridges, *J. Geophys. Res.*, *85*(B12), 7235–7241, doi:10.1029/JB085iB12p07235.

Sandwell, D. T., and G. Schubert (1982), Geoid height-age relation from SEASAT altimeter profiles across the Mendocino Fracture Zone, *J. Geophys. Res.*, *87*(B5), 3949–3958, doi:10.1029/JB087iB05p03949.

Schroeder, W. (1984), The empirical age-depth relation and depth anomalies in the Pacific Ocean basin, *J. Geophys. Res.*, *89*(B12), 9873–9883, doi:10.1029/JB089iB12p09873.

Schubert, G. (1980), Self-driven motions of plates and descending slabs, in *Mechanisms of Plate Tectonics and Continental Drift*, edited by P. A. Davies and S. K. Runcorn, pp. 151–158, Academic, New York.

Schubert, G., C. Froidevaux, and D. A. Yuen (1976), Oceanic lithosphere and asthenosphere: Thermal and mechanical structure, *J. Geophys. Res.*, *81*(20), 3525–3540, doi:10.1029/JB081i020p03525.

Sclater, J. G., and J. Francheteau (1970), The implications of terrestrial heat flow observations on current tectonic and geochemical models of the crust and upper mantle of the Earth, *Geophys. J. R. Astron. Soc.*, *20*, 509–542, doi:10.1111/j.1365-246X.1970.tb06089.x.

Smith, W. H. F., and D. T. Sandwell (1997), Global sea floor topography from satellite altimetry and ship depth soundings, *Science*, *277*, 1956–1962, doi:10.1126/science.277.5334.1956.

Stein, C. A., and S. Stein (1992), A model for the global variation in oceanic depth and heat flow with age, *Nature*, *359*, 123–129, doi:10.1038/359123a0.

Tapley, B. D., S. Bettadpur, M. Watkins, and C. Reigber (2004), The gravity recovery and climate experiment: Mission overview and early results, *Geophys. Res. Lett.*, *31*, L09607, doi:10.1029/2004GL019920.

Turcotte, D. L., and E. R. Oxburgh (1967), Finite amplitude convective cells and continental drift, *J. Fluid Mech.*, *28*, 29–42, doi:10.1017/S0022112067001880.

Turcotte, D., and G. Schubert (2002), *Geodynamics*, 2nd ed., Cambridge Univ. Press, Cambridge, U. K.

Wessel, P., and W. F. Haxby (1989), Geoid anomalies at fracture zones and thermal models for the oceanic lithosphere, *Geophys. Res. Lett.*, *16*, 827–830, doi:10.1029/GL016i008p00827.